Tuning Ni dopant concentration to enable co-deposited superhydrophilic self-standing Mo$_2$C electrode for high-efficient hydrogen evolution reaction

Wei Liu [a,b], Xiting Wang [c], Jiakang Qu [a,b], Xianglin Liu [a,b], Zhaofu Zhang [d], Yuzheng Guo [c,*], Huayi Yin [a,b,**], Dihua Wang [a,b,**]

[a] *International Cooperation Base for Sustainable Utilization of Resources and Energy in Hubei Province, China*
[b] *School of Resource and Environmental Science, Wuhan University, Wuhan 430072, China*
[c] *School of Electrical Engineering and Automation, Wuhan University, Wuhan 430072, China*
[d] *Department of Engineering, Cambridge University, Cambridge CB2 1PZ, United Kingdom*

A R T I C L E I N F O

A B S T R A C T

Ni doping is an effective way to change the electronic structure of molybdenum carbide (Mo$_2$C) to promote the hydrogen evolution reaction (HER) performance. However, the relationship between the Ni dopant concentration and HER activity remains to be explored. Herein, we prepare self-sanding Mo$_2$C electrodes with different Ni concentrations, and employ density functional theory (DFT) calculations along with electrochemical tests to investigate the effect of the Ni dopant concentration on HER activity. The Mo and C come from the co-deposition of MoO$_4^{2-}$ and CO$_3^{2-}$ on a Ni substrate that supplies Ni dopant. The concentration of Ni dopant can be tuned by adjusting the temperature. The HER performance of the Mo$_2$C electrodes with various Ni dopant concentrations is in line with DFT calculations that the optimized Ni-Mo$_2$C-0.67 electrode has a lowest ΔG_{H*} value of -0.13 eV. Altogether, this work sheds light on controllably designing Ni-doped Mo$_2$C electrodes for splitting water.

1. Introduction

Water electrolysis is considered to be the cleanest way to produce hydrogen, and the purity of electrolytic hydrogen (H$_2$) is relatively higher than other methods [1,2]. However, H$_2$ production from electrolyzing water is seriously hindered due to the high HER overpotential and high cost of the precious metal HER catalysts [3]. Platinum (Pt) is considered as an ideal HER catalyst, but its limited reserve and high cost severely limit the large-scale use of Pt-based catalysts [4,5]. Mo$_2$C is one of the most promising materials to replace Pt-based catalysts because of its similar D-band electronic structure to Pt and low cost [6,7]. Enormous efforts have been made to improve the HER performance of Mo$_2$C, such as engineering the particle size [8], morphologies [6] and crystalline phases [9]. However, the HER catalytic activities have not reached expected performances [10,11]. Theoretically, pure Mo$_2$C has a relatively negative hydrogen binding energy (ΔG_{H*}) because of a high density of an empty d orbit of Mo atoms. Thus, it is easy to form strong Mo-H bonds on the surface of Mo$_2$C. But it is not beneficial to the desorption process of active hydrogen atoms, interfering the Heyrovsky/Tafel step.

Elemental doping has been proven to be an effective way to improve the electronic structure of materials. Especially the doping of Ni in Mo$_2$C can promote the H$_2$ desorption process [12]. However, the effect of the concentration of Ni dopant on the HER performance of Ni-doped Mo$_2$C is still unclear.

Recently, Ni-doped Mo$_2$C catalysts have been prepared by various methods to improve the HER performance [12–16]. The solid-state thermolysis method was considered to be an efficient method to prepare Ni-doped MoC/Mo$_2$C [12,13]. The results show that Ni dopant in MoC/Mo$_2$C is superior to other dopants such as Fe, Cr, and Co [13]. In addition, Ni-doped Mo$_2$C has been prepare by hydrothermal method [14–16], and the results indicate that Ni doping can improve the HER performance of Mo$_2$C greatly. The enhanced HER performance of Mo$_2$C can be attributed to the fact that Ni increased electrochemical active surface area (ECSA) and intrinsic HER activity [17,18]. However, we noted that Ni concentration in catalysts was not quantitatively measured among various doping methods. In other words, the concentration of Ni dopant in the catalyst was randomly designed or not known. Thus, the proper Ni dopant concentration is still unclear when designing Ni-doped

---

Mo$_2$C catalysts, which hinders the development of the Ni-doped Mo$_2$C-based HER catalysts. Therefore, it is worthwhile to study the effect of the Ni dopant concentration on the HER performance.

In this paper, we prepared a self-standing Ni-doped Mo$_2$C HER electrode by one-step electrochemical co-deposition of MoO$_4^{2-}$ and CO$_3^{2-}$ in molten LiF-NaF-KF-Na$_2$MoO$_4$-K$_2$CO$_3$ salts. The Ni dopant came from the Ni substrate, and the Ni concentration in the Mo$_2$C can be controlled by adjusting the operating temperature that affects the diffusion rate of Ni in the Mo$_2$C. Unlike the powdery catalysts, the electrolytic self-standing catalytic Ni-doped Mo$_2$C layer was robust and does not need any electrical conducting agent and binder. More importantly, we combined DFT (Density Functional Theory) calculations and electrochemical deposition method to investigate the relationship between the Ni dopant contents in Mo$_2$C and its intrinsic HER activity. The optimized HER electrode (Ni-Mo$_2$C-0.67) showed an excellent HER performance, only requiring 165 mV and 214 mV in 0.5 M H$_2$SO$_4$, 151 mV and 194 mV in KOH to drive $-$ 10 mA cm^{-2} and $-$ 100 mA cm^{-2} HER current density, respectively. And Ni-Mo$_2$C-0.67 exhibited a superior stability with no obvious deterioration in activity after continuous 200 h HER operation at the overpotential of 150 mV.

2. Experimental methods

2.1. Electrodeposition of Ni-Mo$_2$C-x

The self-standing Ni-Mo$_2$C-x catalytic layer was electrodeposited on a Ni plate cathode in molten LiF-NaF-KF (molar ratio 5: 1: 4) with the addition of 1.3 mol% K$_2$CO$_3$ and 1.3 mol% Na$_2$MoO$_4$ at 750–820 °C. All reagents used in the experiment are of analytical grade (>99%, Sinopharm Chemical Reagent Co., Ltd.). First, all reagents were mixed and placed in a graphite crucible that was contained in a stainless steel (SS) reactor, and the mixtures were dried at 300 °C for 24 h in a tube furnace. Second, the SS reactor was flowed with Ar and then heated to target temperature to melt the salts at a ramping rate of 5 °C min^{-1}. Third, the electrodeposition was performed between a Ni plate (10 mm × 10 mm × 0.1 mm) that was polished with 500 mesh silicon carbide sandpaper and the Mo anode under constant current densities (250 mA cm^{-2}) and time (60 min). After each electrodeposition, the Ni plate cathode was lifted out from the molten salts and cooled down to room temperature. Finally, the as-prepared samples were washed by distilled water and ethanol, respectively. The electrodes with different Ni contents prepared at different temperatures were named hereafter as Ni-Mo$_2$C-x, where x is the Ni content obtained from the ICP tests (x is 0.1, 0.2, 0.34 and 0.67 mg L^{-1} in the Ni-Mo$_2$C electrodes prepared at 850 °C, 820 °C, 800 °C and 750 °C). It should be noted that the Ni/Mo atom rates in Ni-Mo$_2$C-0.1, Ni-Mo$_2$C-0.2, Ni-Mo$_2$C-0.34 and Ni-Mo$_2$C-0.67 is about 1/100, 2/94, 4/92 and 8/88. The Ni/Mo atom rates were used for the DFT calculations.

2.2. The preparation of Ni-Mo$_2$C-1.33

The Ni-Mo$_2$C-1.33 catalyst was prepared by the following steps. NiO (9.4 mg), C$_6$H$_{12}$O$_6$ (100 mg) and MoS$_2$ powder (200 mg) were preliminarily mixed by ball milling and then ultrasonically dispersed (200 W, 2 h) in 250 mL distilled water to form a uniform suspension. Subsequently, 15 mL of this suspension was evenly coated on CC (1 × 1 cm^2) in batches. The formed CC/NiO/ C$_6$H$_{12}$O$_6$/MoS$_2$ precursor was dried in air, calcined at 300 °C for 1 h in Ar, and electrolytically reduced (2.6 V, 1 h) in molten NaCl-KCl (700 °C) in the end. The sample after electrolysis was lifted from the molten salts, and washed by distilled water. The obtained sample was named as Ni-Mo$_2$C-1.33 with the Ni content of 1.33 mg L^{-1}.

2.3. Materials characterizations

The morphologies and microstructures of all electrodes were characterized by scanning electron microscopy (SEM, MIRA3) equipped with an energy dispersive X-ray spectroscopy (EDS, Aztec Energy) and transmission electron microscopy (TEM, FEI tecnai G2 F20). Phase compositions of the as-prepared samples were investigated by X-ray diffraction (XRD, Rigaku MiniFlex 600). The valence information of elements in all samples was tested by X-ray photoelectron spectroscopy (XPS ESCALAB 250Xi). The contact angle between electrodes and water was measured on a Dataphysics OCA25 contact angle meter. The content of Ni in the active materials is determined by inductively coupled plasma mass spectrometry (ICP-MS, Analytik Jena AG).

2.4. Measurements of HER performances

HER performances of all electrolytic samples were investigated in 0.5 M H$_2$SO$_4$ and 1 M KOH solutions by a three-electrode system, respectively. A three-electrode system consists of a working electrode made from the electrolytic sample, a graphite rod counter electrode, and a Hg/Hg$_2$SO$_4$ or Hg/HgO reference electrode. Linear sweep voltammetry (LSV), cyclic voltammetry (CV) and chronoamperometric tests were performed to evaluate the HER activity and stability of the working electrode on an electrochemical workstation (CH Instrument, CHI1140C, Shanghai Chenhua Instrument Co. Ltd., China). Electrochemical impedance spectroscopy (EIS) measurements were conducted in a frequency range from 100 kHz to 10 mHz with an AC potential amplitude of 5 mV on an electrochemical workstation (PARSTA2273, AMETEK Scientific Instruments Co. Ltd., America). Prior to each electrochemical measurement, the electrolyte was bubbled with high-purity Ar for over 40 min to remove the dissolved oxygen in the electrolyte. Unless stated otherwise, all potentials in this paper refer to Reversible Hydrogen Electrode (RHE) by adding a value of (0.64 + 0.059 pH) V in 0.5 M H$_2$SO$_4$, and (0.098 + 0.059 pH) V in 1 M KOH with iR compensation.

2.5. DFT calculations

Spin-polarized density functional theory (DFT) calculations were applied by using the Vienna ab initio simulation package (VASP) [18]. The projector-augmented wave (PAW) method was performed to calculate the interaction between the ions and electrons, while the Perdew-Burke-Ernzerhof functional was used to describe the exchange-correlation energy [19,20]. Calculations details were set with 400 eV cutoff energy for plane-wave basis sets. 3 × 3 × 1 Γ-centered Monkhorst-Pack k-point grids were adopted for the first Brillouin zone. The convergence criterias for force and total energy were 0.01 eV/Å and 10^{-5} eV, respectively. The van der Waals (vdW) interactions was treated by DFT-D3 method in Grimme's scheme [21]. Bader charge analysis were performed to analyze the charge distribution [22].

The Gibbs free energy are calculated with the computational hydrogen electrode (CHE) model [23–25]. The reaction free energy change (ΔG) for each elementary step is calculated as

$$\Delta G = \Delta E + \Delta E_{ZPE} - T\Delta S + eU + \Delta G_{pH}$$

where ΔE represents the reaction energy by the corresponding systems. ΔE_{ZPE} is the zero-point energy correction. ΔS is entropy change, T is the temperature (298.15 K), respectively. e and U are the number of transferred electrons and the applied electrode potential, respectively, which are obtained from the applied potential effect. ΔG_{pH} is the pH free energy correction, which is calculated as

$$\Delta G_{pH} = k_B T \times \ln 10 \times pH$$

In this experiment, we calculated the ΔG_{H*} values of the Mo$_2$C catalysts with different Ni/Mo atom rates of 0/96, 2/94, 8/88, 10/86, 12/84 and 16/80. The Mo$_2$C catalysts with the Ni/Mo atom rates of 2/94, 8/88, 12/84 corresponds to the Ni-Mo$_2$C-0.2, the Ni-Mo$_2$C-0.67 and the Ni-Mo$_2$C-1.33 electrodes (prepared details are shown in ESI) with the Ni/Mo atom rate of 12/84, respectively.

3. Results and discussion

3.1. Ni-Mo₂C electrodes synthesis and characterization

As shown in Fig. S1a, the theoretical decomposition voltage of CO_3^{2-} to C is close to that of MoO_4^{2-} to Mo, which indicates that CO_3^{2-} and MoO_4^{2-} can be reduced to C and Mo at a close potential from the thermodynamic calculations. The LSV curves (Fig. S1b) of Ni electrode in LiF-NaF-KF-Na₂MoO₄ (1.3 mol%) and LiF-NaF-KF-K₂CO₃ (1.3 mol%) also indicate that CO_3^{2-} and MoO_4^{2-} can be reduced at a close potential. Further, we carried out the electrolysis on the surface of Ni sheet in molten LiF-NaF-KF-Na₂MoO₄ (1.3 mol%)-K₂CO₃ (1.3 mol%) at a constant potential of − 0.75 V for 1 h (Fig. S1c). Clearly, the Ni sheet electrode became black from original glossy metal color after electrolysis (Fig. S2a-b). The obtained sample was Mo₂C (Fig. S2c). Thus, CO_3^{2-} and MoO_4^{2-} can be co-reduced to Mo and C.

Unlike the conventional electrodeposition process, the Ni-Mo₂C electrode preparation process contains three steps that happen simultaneously including the co-reduction process of CO_3^{2-} and MoO_4^{2-}, the alloying process of deposited Mo and C atoms and the diffusion of Ni into the Mo₂C layer (Fig. 1a). During the electrochemical deposition process,

the electrochemical reduction of CO_3^{2-} at the cathode generated C while releasing O^{2-} that is consumed by the carbonization of CO_2 to replenish CO_3^{2-} (CO_3^{2-} + 4e⁻ = C + 3 O^{2-}, O^{2-} + CO_2 = CO_3^{2-})[26]. The electrochemical reduction of MoO_4^{2-} shows a similar process to that of CO_3^{2-}. The electrochemical reduction of MoO_4^{2-} produced Mo and released O^{2-} that is transferred to the anode and react with Mo ions to form MoO_4^{2-}. The active Mo and C atoms co-deposited on the surface of the cathode further reacted to form Mo₂C. Thus, the so-called co-deposited reaction employs CO_2 as the carbon source and Mo rods as molybdenum source and electrons as the reducing agent, laying a simple, effective and sustainable way to utilize CO_2 as a valuable feedstock. At the same time, the Ni atoms in the Ni substrate tend to diffuse out at high temperatures and react with co-deposited Mo and C atoms to form Ni-doped Mo₂C. Clearly, the Ni sheet with a metallic luster turned to black with a rough surface, indicating that a uniform and rough layer was deposited on its surface. Adjusting the experimental temperature, the roughness of the deposited materials on the Ni surface gradually decreases as the temperature increases (Fig. S3). Thus, electrochemical co-deposition is a powerful method to prepare the Mo₂C self-standing electrode with controlled Ni dopant concentrations for the use of efficient and durable HER catalysts.
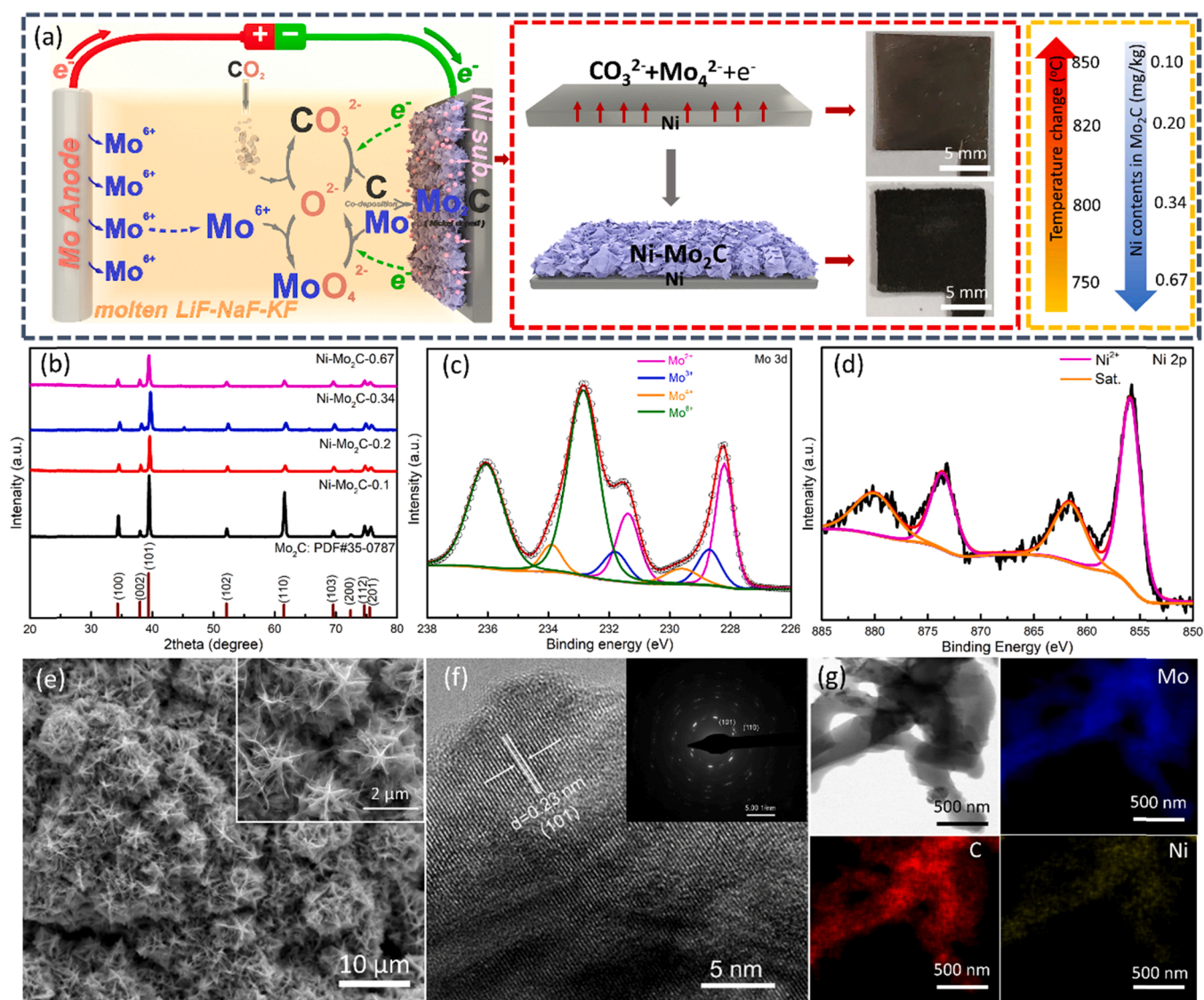

Fig. 1. Materials synthesis and characterization. (a) Schematic of preparing the Ni-Mo₂C-0.67 electrode in molten carbonate and digital pictures of the Ni electrode before and after electrolysis. (b) XRD pattern of different electrodes. XPS patterns (c-d), SEM images (e), HRTEM images (f), HAADF-STEM image and the corresponding EDS mapping (g) of the Ni-Mo₂C-0.67 electrode.

All samples are consistent in XRD peak position (34.4 °, 38.0 °, 39.4 °), which are indexed to the 100, 002, 101 planes of Mo_2C (JCPDS, No. 35–0787). Notably, the peak intensity of Mo_2C gradually increases and the peak width gradually decreases with increasing temperature, indicating the presence of abundant smaller crystallites in samples prepared at low temperature. More Mo_2C crystallites can provide more HER active sites and charge transfer channels. XPS results of Mo 3d indicate that there are four kinds of Mo species (Mo^{2+}, Mo^{3+}, Mo^{4+} and Mo^{6+}) [27,28]. Mo^{2+} and Mo^{3+} originate from Mo-C in Mo_2C coating, and Mo^{4+} and Mo^{6+} species derive from MoO_2 and MoO_3 that are often observed at the surface of Mo_2C when exposed to water or air [13, 29–31]. The high-resolution Ni 2p XPS spectra (Fig. 1d) indicate Ni has been doped into the prepared Mo_2C coating successfully. [12,13] And the content of doped Ni decreases from 0.67 to 0.1 mg L^{-1} with the temperature changing from 750 to 850 °C (Table S1). The cross-sectional SEM images (Fig. S4) of the four electrodes indicate that a lower operating temperature is conducive to the preparation of thicker and more porous coatings. Besides, ICP results show that the content of Ni dopant decreases with increasing the operating temperature. At a higher temperature, more carbon dissolves in Ni to form a carbon-enriched transition layer that will prevent the Ni diffusion from the substrate to the Mo_2C layer [32]. The SEM image in Fig. 1e indicates that the Mo_2C layer has abundant 3D flower-like porous architectures.

At the microscale, there exist 3 D flower-like porous architectures which can endow the self-supporting electrode with a large specific surface area providing more active sites. In addition, this 3D structure may allow liquid electrolyte to reach the catalytic surface due to the strong capillary forces [33]. This can shorten the diffusion paths of electrolyte and generated bubbles and thereby accelerate the pace of the electrolyte to the active sites and the departure of the generated gas during HER. The Mo_2C nanosheets structures were also confirmed by TEM image (Fig. S5). HRTEM image along with the corresponding selected area electron diffraction (SAED) pattern (Fig. 1f) and the EDS images (Fig. 1g) confirm the generation of Ni-doped Mo_2C, which agrees well with the XRD patterns. Overall, the Ni-doped Mo_2C electrodes with different micro-topographies and Ni contents can be obtained by turning the electrolysis temperature (high temperature is beneficial to form denser microstructures with lower Ni doped) (Fig. S6).

3.2. Electrocatalystic HER performance

The HER performances of electrolytic self-standing Ni-Mo_2C electrodes were evaluated in both 0.5 M H_2SO_4 and 1 M KOH solutions. As shown in Fig. 2a, the Ni-Mo_2C-0.67 electrode only requires a small overpotential of 165 mV and 214 mV to reach a geometric current density (j) of 10 mA cm^{-2} and 100 mA cm^{-2} in H_2SO_4 solution. The
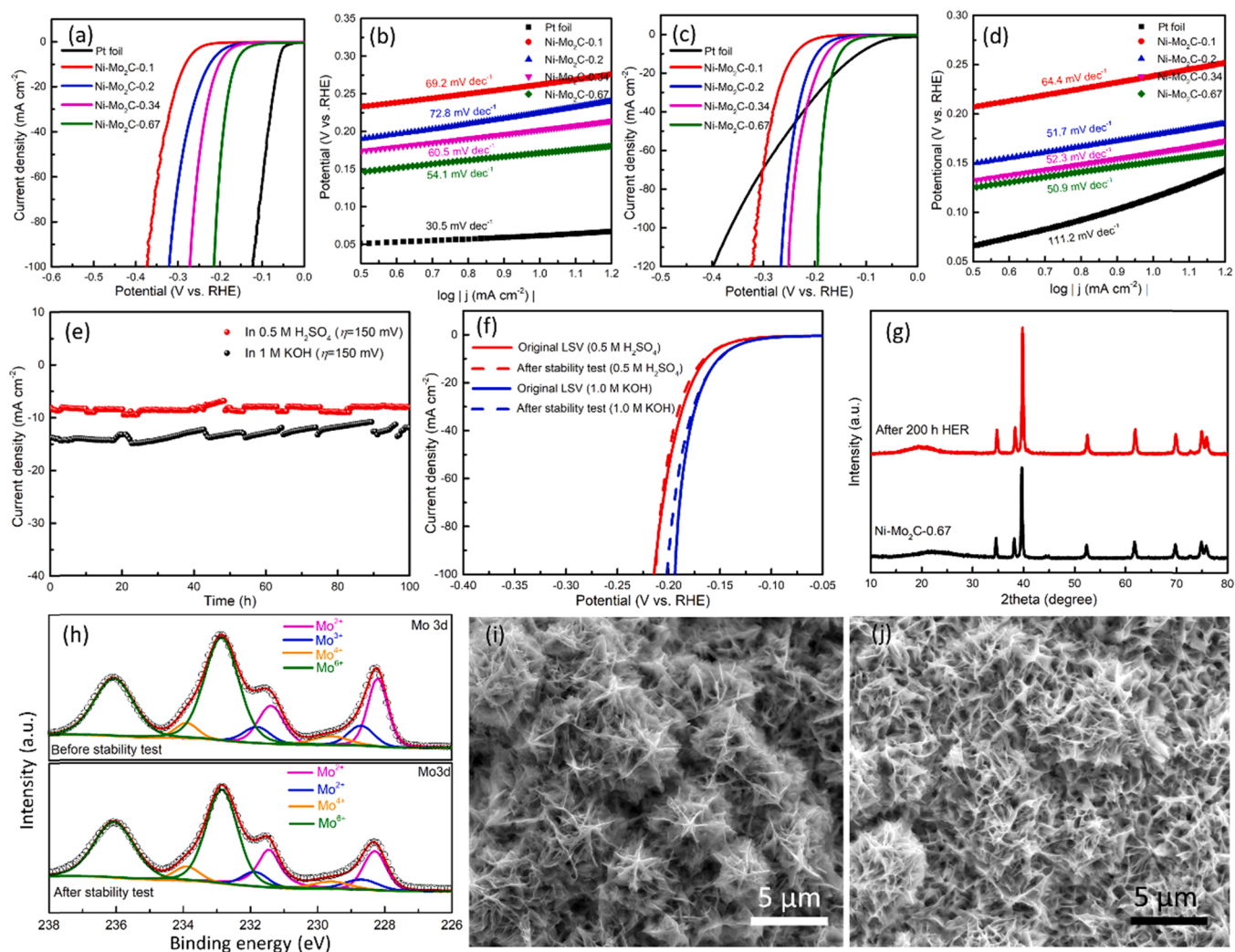

Fig. 2. HER performances of the electrolytic electrodes. The polarization curve (a) and the Tafel plots (b) in 0.5 M H_2SO_4 solution, the polarization curve (c) and the Tafel plots (d) in 1.0 M KOH solution. The long-term electrolysis stability tests (e) of the Ni-Mo_2C-0.67 electrode at η = 150 mV in 0.5 M H_2SO_4 and 1 M KOH, respectively. Polarization curves before and after stability tests (f), XRD patterns (g), XPS patterns (h) and SEM images (i-j) of the Ni-Mo_2C-0.67 electrode before and after stability tests for continuous 200 h.

overpotentials of the Ni-Mo$_2$C-0.67 electrode are much lower than that of Ni-Mo$_2$C-0.34, Ni-Mo$_2$C-0.2 and Ni-Mo$_2$C-0.1 electrodes as well as the data of most of self-standing noble metal-free HER electrodes in the literatures (for details see Table S2, S3). Accordingly, the Tafel plots (Fig. 2b) derived from the polarization curves imply that the Ni-Mo$_2$C-0.67 electrode has a relatively small Tafel slope value of 54.1 mV dec^{-1}, which is only smaller than Pt among all electrolytic samples (60.5 mV dec^{-1} for Ni-Mo$_2$C-0.34, 72.8 mV dec^{-1} for Ni-Mo$_2$C-0.2 69.2 mV dec^{-1} for Ni-Mo$_2$C-0.1). This indicates that Ni-Mo$_2$C-0.67 has the most favorable HER kinetics. Until today, few Mo$_x$C based HER catalysts can work well in both acidic and alkaline solution. Herein, the HER activity of the Ni-Mo$_2$C-0.67 electrode in 1 M KOH was further evaluated by polarization curves (Fig. 2c) and Tafel plot (Fig. 2d). The Ni-Mo$_2$C-0.67 electrode gets the current densities of 10 mA cm^{-2} and 100 mA cm^{-2} at small overpotentials of 151 mV and 194 mV with a Tafel slope value of 50.9 mV dec^{-1}, verifying the outstanding activity among the current reported self-standing noble metal-free HER electrodes (Table S4, S6). Although Pt electrode has a smaller HER overpotential in the current density range of below 20 mA cm^{-2}, the Ni-Mo$_2$C-0.67 electrode shows better HER performance than that of Pt electrode at the high current density range from 20 to 100 mA cm^{-2}. And the HER performance of the Ni-Mo$_2$C-0.67 electrode is better than that of other Mo$_2$C based materials obtained by molten salts electrolysis [34–36] and most of HER catalysts that have been reported (Table S5). The Nyquist plots also confirm that the Ni-Mo$_2$C-0.67 electrode has a small charge transfer

resistance at various applied overpotentials (Fig. S7). At $\eta = 150$ mV, the Ni-Mo$_2$C-0.67 electrode shows the lowest charge-transfer resistance value (R$_{ct}$ =1.41 Ω) in comparison with other electrolytic electrodes (2.23 Ω for Ni-Mo$_2$C-0.34, 2.7 Ω for Ni-Mo$_2$C-0.2 and 13.73 Ω for Ni-Mo$_2$C-0.1) (Fig. S7, S8, S9, Table S2). Therefore, the Ni-Mo$_2$C-0.67 electrode with abundant flower-like porous architectures and higher contents of Ni has more excellent HER performance.

Besides its excellent HER activity, the Ni-Mo$_2$C-0.67 electrode also exhibits a good catalytic stability. As shown in Fig. 2e, the Ni-Mo$_2$C-0.67 electrode shows an almost constant catalytic current for 200 h in both 0.5 M H$_2$SO$_4$ and 1 M KOH. Both of the polarization curves of Ni-Mo$_2$C-0.67 in 0.5 M H$_2$SO$_4$ and 1 M KOH after 200 h stability remain nearly unchangeable (Fig. 2f). The composition and surface topography of Ni-Mo$_2$C-0.67 before and after the durability measurement were compared to investigate the reasons for the super stability of Ni-Mo$_2$C-0.67. There are no obvious changes in XRD diffraction peaks (Fig. 2g) and XPS spectra (Fig. 2h) after stability tests. In addition, the surface of Ni-Mo$_2$C-0.67 still retains the 3D porous architectures intact after stability test (Figs. 2i, 2j). The 3D porous architectures are beneficial to the separation of generated H$_2$ gas, avoiding gas blockages and reducing erosion of the pore walls by the gas. All the above results prove that the Ni-Mo$_2$C-0.67 electrode has a super strong HER stability.
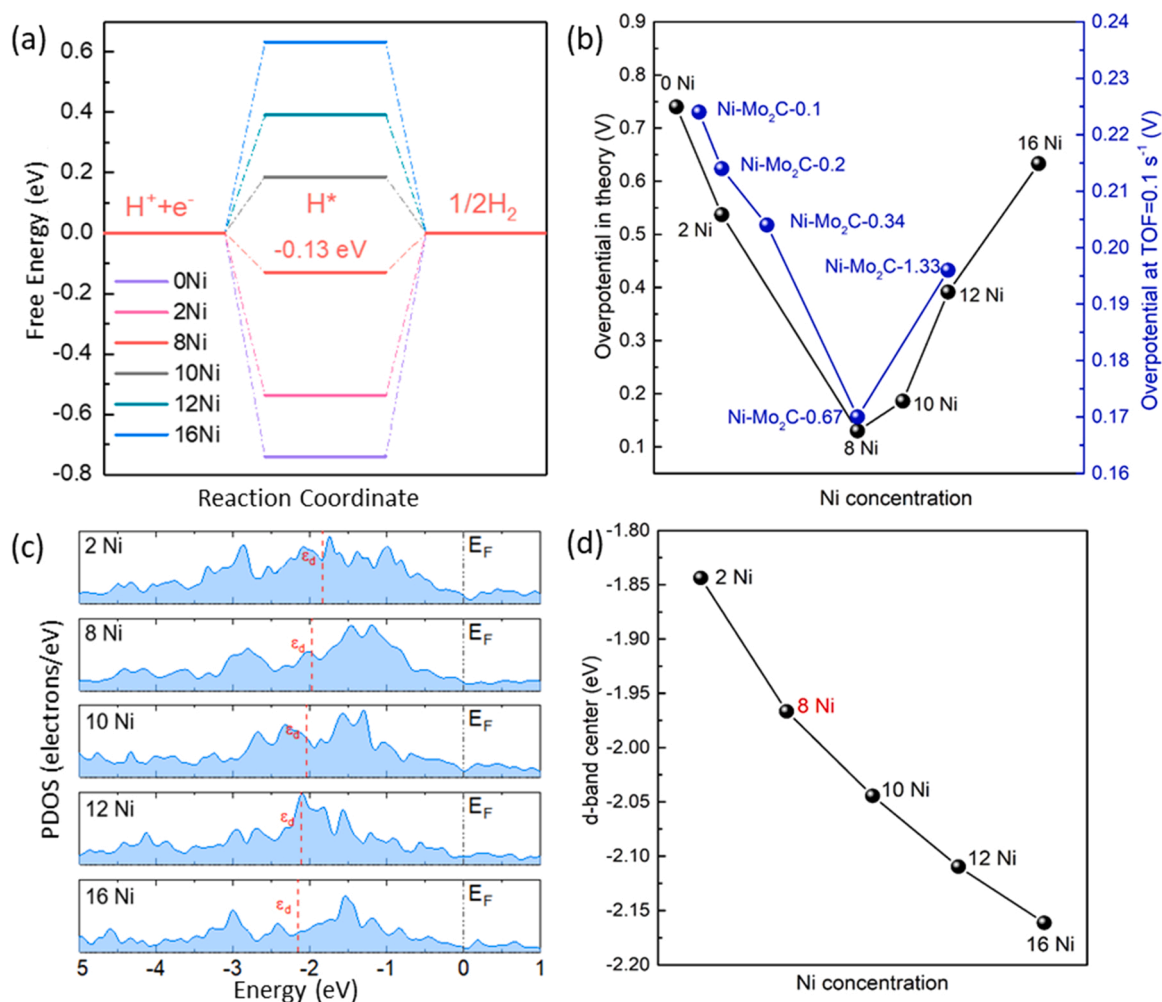

Fig. 3. The DFT calculation details. (a) Calculated HER free-energy diagrams for xNi-Mo$_2$C (x = 0, 2, 8, 10, 12, and 16); (b) the HER overpotential of xNi-Mo$_2$C in theory and overpotential of different electrodes (Ni-Mo$_2$C-0.1, Ni-Mo$_2$C-0.2, Ni-Mo$_2$C-0.0.34, Ni-Mo$_2$C-0.67 and Ni-Mo$_2$C-1.33) at the TOF values of 0.1 s^{-1}; (c) the projected density of states (PDOS) of the Ni-d orbitals in xNi-Mo$_2$C; (d) D-band center of xNi-Mo$_2$C.

3.3. DFT theoretical investigation

To understand the possible mechanism for HER, DFT calculations were performed to investigate the influence of Ni doping in Mo_2C for the HER. The pure Mo_2C and Ni-doped Mo_2C ($xNi-Mo_2C$, x = 0, 2, 8, 10, 12, and 16) are constructed, as shown in Fig. S10. The $2Ni-Mo_2C$, $8Ni-Mo_2C$ and $12Ni-Mo_2C$ correspond to the $Ni-Mo_2C-0.2$, $Ni-Mo_2C-0.67$ and $Ni-Mo_2C-1.33$, respectively. When x = 16, Ni atoms replace all Mo atoms on the Mo_2C surface. Notably, it is energetically favorable for Ni atoms to replace the surface Mo atoms (Fig. S11). An ideal HER catalyst should exhibit an approximately zero free energy of adsorbed H* ($\Delta G_{H*} \approx 0$), which can guarantee the optimal catalytic ability to adsorb H proton and simultaneously to release H_2 easily. As shown in Fig. 3(a), the ΔG_{H*} of pure Mo_2C ($0Ni-Mo_2C$) is $- 0.74$ eV. The strong interaction between the adsorbed H proton and Mo_2C will prohibit the release of H_2, leading to the poor HER activity. When Ni atoms are doped, the hydrogen adsorption/desorption process differs from the Ni doping concentration to concentration. The values of ΔG_{H*} on $xNi-Mo_2C$ become positive with the increase of Ni doping concentration. The H* adsorption is strong when Ni doping concentration is low (i.e., $2Ni-Mo_2C$), while the over-much Ni doping (i.e., $16Ni-Mo_2C$) will lead to the weak H* adsorption. Correspondingly, as seen in Fig. 3(b), the HER overpotentials decrease first and then increase, resulting in the optimal HER performance on $8Ni-Mo_2C$ ($\Delta G_{H*} = -0.13$ eV), which is consistent with the results obtained from electrochemical tests. Thus, it is demonstrated that the moderate Ni-doped Mo_2C can enhance HER activity, which is consistent with the experimental observation.

Moreover, the electronic structures of $xNi-Mo_2C$ are analyzed to better understand the influence of Ni doping on HER catalytic performance. The projected density of states (PDOS) of the Ni-d orbitals in $xNi-Mo_2C$ is plotted in Fig. 3(c). It is found that the electronic structures of $xNi-Mo_2C$ redistribute after Ni doping, due to the different electronegativity between Ni (1.91) and Mo atoms (1.16). Thus, the values of the D-band center decrease gradually as the Ni doping concentration increases (Fig. 3(d)). The downshift of the D-band center can weaken the ability of H* adsorption. Thus, by rationally tuning the d band center, $xNi-Mo_2C$ can obtain the HER optimal catalytic performance with moderate Ni doping concentration.

From the above DFT results, the $Ni-Mo_2C$ catalyst with the moderate Ni/Mo atom rate of 8/88 has an optimal ΔG_{H*} value. For a HER catalyst, the intrinsic catalytic ability is important for the HER performance. The turnover frequency (TOF) at a specific overpotential is a useful parameter to estimate the intrinsic activity of catalyst. The TOF results (Fig. S12) indicate that the $Ni-Mo_2C-0.67$ electrode with the moderate Ni/Mo atom rate of 8/88 has the largest TOF value at the same potential. This indicates that the $Ni-Mo_2C-0.67$ electrode has a superior intrinsic activity and doping more Ni in Mo_2C is beneficial to improve its HER performance. Note that the HER performance of the $Ni-Mo_2C$ electrodes increases with increasing the Ni content. To find out an optimal doped Ni content, we further increase Ni dopant concentration in the Mo_2C electrode by electrochemical solid state reduction method in molten NaCl-KCl salts (see details in ESI). The concentrations of Ni and Mo in the as-prepared $Ni-Mo_2C-1.33$ were measured (Table S1). The Ni concentration in the electrolytic Mo_2C is 1.33 mg L^{-1} with the Ni/Mo atom rate of about 12/84, which is higher than that of $Ni-Mo_2C-0.67$. In addition, we note that the HER performance of $Ni-Mo_2C-1.33$ in 0.5 M H_2SO_4 is better than the $Ni-Mo_2C-0.67$ (Fig. S13), and its C_{dl} value is also larger than that of $Ni-Mo_2C-0.67$ (Fig. S12, Fig. S14). This means that the intrinsic HER activity of $Ni-Mo_2C-1.33$ is inferior to $Ni-Mo_2C-0.67$ (Fig. S12). The above results indicate that the intrinsic HER activity of electrodes increases first with the increasing of Ni concentration, and then decreases when the atom rate of Ni/Mo exceeds 8/88. The experimental results agree well with DFT calculations that the optimal Ni dopant concentration is around 8/88, which is very helpful to the design and preparation of carbides HER catalysts.

3.4. Surface properties investigation

The wettability between HER electrodes surface and water also affects H_2 bubbles' motion behaviors that may determine the kinetics of the HER performance [37,38]. In general, it's better to form more uniform and smaller H_2 bubbles that can leave from the electrode without causing high polarization of HER electrodes. In general, the contact angle is a useful data that can reflect the hydrophilicity of the electrodes. The contact angles of Pt, $Ni-Mo_2C-0.67$, $Ni-Mo_2C-0.34$, $Ni-Mo_2C-0.2$ and $Ni-Mo_2C-0.1$ electrodes are 76 °, 0 °, 7 °, 21 ° and 59 ° (Fig. 4), respectively. The contact angle value of $Ni-Mo_2C-0.67$ is 0, which demonstrates the excellent wettability between $Ni-Mo_2C$ electrodes and water. An in-situ video confirms its super-hydrophilic nature of the $Ni-Mo_2C-0.67$ electrode (Video S1). The super-hydrophilic nature may be attributed to their more 3D flower-like nano-porous architectures with open channels/pores [39–41], which promote electrolyte to reach active catalytic sites and benefit the bubbles separation [38,40].

Supplementary material related to this article can be found online at doi:10.1016/j.apcatb.2022.121201.

In addition, the recorded videos were used to compare the size distributions and the dynamics of the release of H_2 bubbles on Pt and all $Ni-Mo_2C$ electrodes. Clearly, H_2 bubbles strongly adhere to the Pt surface and grow to very large size ($\sim 60\% > 700$ μm), thus covering most active sides on the Pt foil and slowing down the mass transfer rate at the interface of electrode/electrolyte (Video S2, Fig. 4a). In contrast, the H_2 bubbles on the surface of the $Ni-Mo_2C-0.67$ electrode generate and leave instantly (Video S3). This indicates that the shielding effect caused by generated H_2 bubbles on the surface of $Ni-Mo_2C-0.67$ is not obvious (Fig. 4b) when the size of the bubbles is less than 300 μm in diameter. In addition, the generation and growth process of H_2 bubbles were observed clearly on the surface of $Ni-Mo_2C-0.34$, $Ni-Mo_2C-0.2$ and $Ni-Mo_2C-0.1$ (Video S4–6, Fig. 4c-e). Thus, the bubbles on the electrode having a better hydrophilicity can departure more easily, thereby maintaining the constant exposure of catalytic sites and retaining an effective and stable HER activity. According to the solid-liquid-gas interface theory, roughness at both the micro- and nano-scale structures not only generates a strong capillary force to pump liquid, but also reduces interfacial adhesion to facilitate gas bubble release [42,43].

Supplementary material related to this article can be found online at doi:10.1016/j.apcatb.2022.121201.

The surface property is a parameter to determine the HER performance. The cyclic voltammetry was used to get the double-layer capacitances (C_{dl}) and calculate the ECSA values of all $Ni-Mo_2C$ HER electrodes (calculation details are given in ESI) [44,45]. All CV curves show a nearly rectangular shape, which implies the high electrical conductivity of $Ni-Mo_2C$ HER electrodes [46]. The C_{dl} values of $Ni-Mo_2C$ HER electrodes are obtained from the slopes, which are 66.7 mF cm^{-2} for $Ni-Mo_2C-0.67$, 34.8 mF cm^{-2} for $Ni-Mo_2C-0.34$, 23.8 mF cm^{-2} for $Ni-Mo_2C-0.2$ and 2.7 mF cm^{-2} for $Ni-Mo_2C-0.1$ (Fig. S15, Fig. S16). Calculated ECSA (Table S6) are to be 1667.5 cm^2, 870 cm^2, 595 cm^2 and 67.5 cm^2, respectively. Thus, the $Ni-Mo_2C-0.67$ electrode has the largest ECSA, which is consistent with its best HER catalytic performance.

Overall, the optimistic hydrophilicity of the $Ni-Mo_2C-0.67$ electrode can promote liquid electrolyte and gas transfer and its largest electrochemical active surface area provides more HER active sites, both of which improve the HER performance of the $Ni-Mo_2C-0.67$ electrode.

4. Conclusion

We combined DFT calculations and the electrochemical co-deposition method to exploit the effect of Ni dopant concentration on the HER performance of Mo_2C electrocatalyst. The Ni concentrations in the electrodeposited self-standing Mo_2C HER electrode can be tuned by adjusting the operating temperature. The optimal Ni dopant concentration is around 0 67 mg L^{-1} that is predicated by DFT calculations and verified by the electrochemical measurement of different Mo_2C
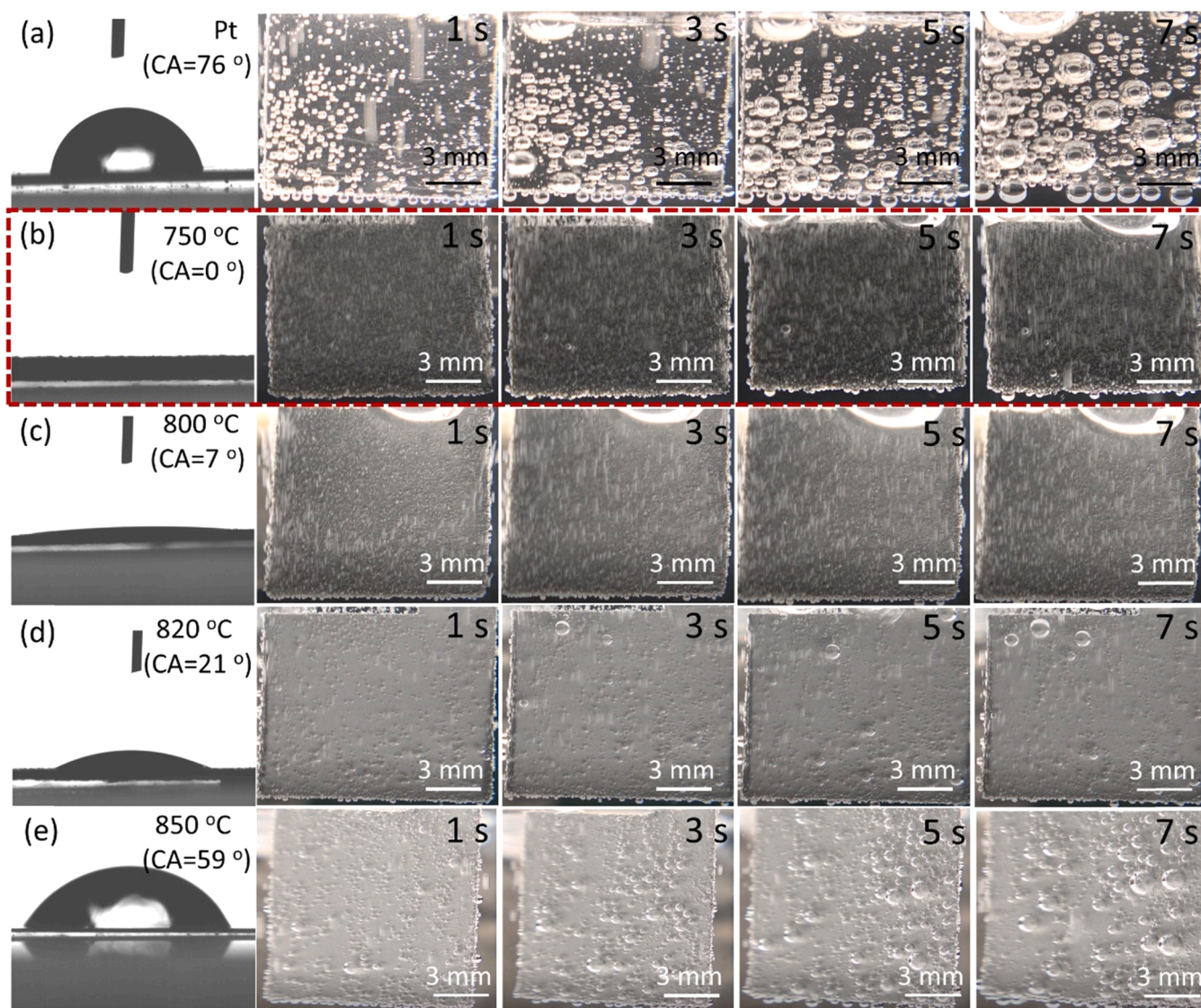
Fig. 4. Contact angle images between water and electrodes and the bubble evolution process on the surface of electrodes at 50 mA cm^{-2} in 0.5 M H$_2$SO$_4$. (a) Pt electrode. (b) The Ni-Mo$_2$C-0.67 electrode. (c) The Ni-Mo$_2$C-0.34 electrode. (d) The Ni-Mo$_2$C-0.2 electrode. (e) The Ni-Mo$_2$C-0.1 electrode.

electrode with varied Ni dopant concentrations. The electrodeposited Ni-Mo$_2$C-0.67 HER electrode has a low overpotentials of 165 mV at $-$ 10 mA cm^{-2} and 214 mV at $-$ 100 mA cm^{-2} in 0.5 M H$_2$SO$_4$, and of 151.1 mV at 10 mA cm^{-2} and 193.8 mV at $-$ 100 mA cm^{-2} in 1 M KOH. The outstanding HER performance is attributed to the suitable Ni dopant concentration, large electrochemical surface area, and excellent hydrophilic characteristics. Moreover, this Ni-Mo$_2$C-0.67 HER electrode lasted for 200 h without no obvious degradation. Overall, this paper reveals the relationship between the Ni dopant concentration and the HER performance of the Mo$_2$C-based catalysts, shedding light on guiding the design of high-performance Ni-doped carbide HER catalysts.

CRediT authorship contribution statement

Dihua Wang: Conceptualization, Methodology. **Huayi Yin:** Methodology, Writing – review & editing. **Wei Liu:** Data curation, Methodology, Writing – original draft. **Jiakang Qu:** Methodology. **Xiting Wang:** Software, Validation. **Yuzheng Guo:** Software, Validation. **Xianglin Liu:** Methodology. **Zhaofu Zhang:** Writing – review & editing.

Declaration of Competing Interest

Authors have no competing interests to declare.

Appendix A. Supporting information

Supplementary data associated with this article can be found in the online version at doi:10.1016/j.apcatb.2022.121201.

References

[1] J. Nai, Y. Lu, L. Yu, X. Wang, D. Lou, Adv. Mater. 29 (2017), 1703870.
[2] L. Yang, L. Zeng, H. Liu, Y. Deng, Z. Zhou, J. Yu, H. Liu, Appl. Catal. B Environ. 249 (2019) 98–105.
[3] C. Tang, N. Cheng, Z. Pu, W. Xing, X. Sun, Angew. Chem. Int. Ed. 54 (2015) 9351–9355.
[4] X. Zou, Y. Zhang, Chem. Soc. Rev. (2014) 5148–5180.

[5] M.S. Faber, S. Jin, Energy Environ. Sci. 7 (2014) 3519–3542.
[6] L. Liao, S. Wang, J. Xiao, X. Bian, Y. Zhang, M.D. Scanlon, X. Hu, Y. Tang, B. Liu, H. H. Girault, Energy Environ. Sci. 7 (2014) 387–392.
[7] H. Vrubel, X. Hu, Angew. Chem. Int. Ed. 51 (2012) 12703–12706.
[8] Y. Liu, G. Yu, G. Li, Y. Sun, T. Asefa, W. Chen, X. Zou, Angew. Chem. Int. Ed. 127 (2015) 10902–10907.
[9] C. Wan, Y.N. Regmi, B.M. Leonard, Angew. Chem. Int. Ed. 53 (2014) 6407–6410.
[10] H. Sun, Z. Yan, F. Liu, W. Xu, F. Cheng, J. Chen, Adv. Mater. 32 (2019), 1806326.
[11] J.A. Majeed, X. Li, P.X. Hou, H. Tabassum, L. Zhang, C. Liu, H.M. Cheng, Appl. Catal. B Environ. 269 (2020), 118823.
[12] S. Wang, J. Wang, M. Zhu, X. Bao, B. Xiao, D. Su, H. Li, Y. Wang, J. Am. Chem. Soc. 137 (2015) 15753–15759.
[13] F. Yu, Y. Gao, Z. Lang, Y. Ma, L. Yin, J. Du, H. Tan, Y. Wang, Y. Li, Nanoscale 10 (2018) 6080–6087.
[14] Z. Hu, L. Zhang, J. Huang, Z. Feng, Q. Xiong, Z. Ye, Z. Chen, X. Li, Z. Yu, Nanoscale 13 (2021) 8264–8274.
[15] C. Liu, L. Sun, L. Luo, W. Wang, H. Dong, Z. Chen, ACS Appl. Mater. Interfaces 13 (2021) 22646–22654.
[16] K.K. Aruna, R. Manoharan, J. Nanopart. Res. 19 (2017) 203.
[17] Y. Ma, G. Guan, P. Phanthong, X. Hao, W. Huang, A. Tsutsumi, K. Kusakabe, A. Abudula, J. Phys. Chem. C 118 (2014) 9485–9496.
[18] G. Kresse, J. Furthmüller, Phys. Rev. B Conden. Matter 54 (1996) 11169–11186.
[19] P.E. Blochl, Phys. Rev. B 50 (1994) 17593–17979.
[20] J.P. Perdew, K. Burke, M. Ernzerhof, Phys. Rev. Lett. 77 (1996) 3865–3868.
[21] S. Grimme, J. Comput. Chem. 27 (2006) 1787–1799.
[22] W. Tang, E. Sanville, G. Henkelman, J. Phys. Conden. Matter 21 (2009) 84204.
[23] J.K. Nørskov, J. Rossmeisl, A. Logadottir, L. Lindqvist, J.R. Kitchin, T. Bligaard, H. Jónsson, J. Phys. Chem. B 108 (2004) 17886–17892.
[24] J.K. Nørskov, T. Bligaard, A. Logadottir, J.R. Kitchin, J.G. Chen, S. Pandelov, U. Stimming, J. Electrochem. Soc. 3 (2005) J23–J26.
[25] A.A. Peterson, F. Abild-Pedersen, F. Studt, J. Rossmeisl, J.K. Nørskov, Energy Environ. Sci. 3 (2010) 1311.
[26] H. Yin, X. Mao, D. Tang, W. Xiao, L. Xing, H. Zhu, D. Wang, D.R. Sadoway, Energy Environ. Sci. 6 (2013) 1538.
[27] L. He, W. Zhang, Q. Mo, W. Huang, L. Yang, Q. Gao, Angew. Chem. Int. Ed. 59 (2020) 3544–3548.
[28] J. Li, Y. Wang, C. Liu, S. Li, Y. Wang, L. Dong, Z. Dai, Y. Li, Y. Lan, Nat. Commun. 7 (2016) 11204.
[29] J. Staszak-Jirkovský, C.D. Malliakas, P.P. Lopes, N. Danilovic, S.S. Kota, K. Chang, B. Genorio, D. Strmcnik, V.R. Stamenkovic, M.G. Kanatzidis, N.M. Markovic, Nat. Mater. 15 (2016) 197–203.
[30] Y. Chen, Y. Zhang, X. Zhang, T. Tang, H. Luo, S. Niu, Z.L. Dai, J. Hu, Adv. Mater. 29 (2017), 1703311.
[31] J. Zhang, T. Wang, P. Liu, Z. Liao, S. Liu, X. Zhuang, M. Chen, E. Zschech, X. Feng, Nat. Commun. 8 (2017) 15437.
[32] J.J. Lander, H.E. Kern, A.L. Beach, J. Appl. Phys. 23 (1952) 1305–1309.
[33] Y. Luo, X. Gong, Y. Chen, J. Zhu, J. Wei, X. Gao, ChemNanoMat 2 (2016) 1018–1022.
[34] Y. Chen, B. Gao, M. Wang, X. Xiao, A. Lv, S. Jiao, P.K. Chu, Nano Energy 90 (2021), 106533.
[35] R. Jiang, L. Pi, B. Deng, L. Hu, X. Liu, J. Cui, X. Mao, D. Wang, ACS Appl. Mater. Interfaces 11 (2019) 38606–38615.
[36] R. Jiang, B. Deng, L. Pi, L. Hu, D. Chen, Y. Dou, X. Mao, D. Wang, ACS Appl. Mater. Interfaces 12 (2020) 57870–57880.
[37] S.H. Ahn, I. Choi, H. Park, S.J. Hwang, S.J. Yoo, E. Cho, H. Kim, D. Henkensmeier, S.W. Nam, S. Kim, J.H. Jang, Chem. Commun. 49 (2013) 9323.
[38] A.K. Kota, Y. Li, J.M. Mabry, A. Tuteja, Adv. Mater. 24 (2012) 5838–5843.
[39] M. Wang, X. Yu, Z. Wang, X. Gong, Z. Guo, L. Dai, J. Mater. Chem. A 5 (2017) 9488–9513.
[40] X. Yu, M. Wang, Z. Wang, X. Gong, Z. Guo, Electrochim. Acta 211 (2016) 900–910.
[41] W. Liu, X. Wang, F. Wang, K. Du, Z. Zhang, Y. Guo, H. Yin, D. Wang, Nat. Commun. 12 (2021) 6776.
[42] Y. Luo, J. Li, J. Zhu, Y. Zhao, X. Gao, Angew. Chem. Int. Ed. 54 (2015) 4876–4879.
[43] J. Li, W. Zhang, Y. Luo, J. Zhu, X. Gao, ACS Appl. Mater. Interfaces 7 (2015) 18206–18210.
[44] A.M. Gómez Marín, E.A. Ticianelli, Appl. Catal. B Environ. 209 (2017) 600–610.
[45] Z. Pu, S. Wei, Z. Chen, S. Mu, Appl. Catal. B Environ. 196 (2016) 193–198.
[46] R. Ge, J. Huo, T. Liao, Y. Liu, M. Zhu, Y. Li, J. Zhang, W. Li, Appl. Catal. B Environ. 260 (2020), 118196.